Int. J. Electrochem. Sci., 17 **(2022)** Article Number: 220338, doi: 10.20964/2022.03.29

International Journal of
ELECTROCHEMICAL
SCIENCE
www.electrochemsci.org

One-step Hydrothermal Synthesis of Amorphous Nickel/Iron Oxide and its Application as Catalyst for Efficient Oxygen Evolution Reaction

Yunfei Li[1,2], Yuanfeng Gao[1,2], Meitang Liu[1,2,], Tianlei Wang[3], Xu Wang[1,2], Haisheng Hu[1,2]*

[1] Beijing Key Laboratory of Materials Utilization of Nonmetallic Minerals and Solid Wastes, PR China.
[2] School of Materials Science and Technology, China University of Geosciences, Beijing, 100083, PR China.
[3] School of Materials Science and Engineering, Tianjin Chengjian University, Tianjin 300384, China
[*]E-mail: Mtliu@cugb.edu.cn.

Received: 8 December 2021 / *Accepted:* 11 January 2022 / *Published:* 2 February 2022

It is of great significance to explore low-cost and high-efficiency oxygen evolution reaction electrocatalysts to meet the challenges of sustainable energy development. In this paper, amorphous nickel-iron oxide was successfully synthesized via a simple one-step hydrothermal method with the help of citric acid-sodium citrate buffer solution and template CTAB. Excellent dispersion and porous structure were found for the obtained samples, which significantly increase the exposed surface area of active sites of the catalyst. In addition, the morphology of Ni-Fe oxides could be controlled and the electronic structure of Ni could be modified by changing Ni/Fe mole ratio. When Ni/Fe mol ratio equals 3:1, this material exhibits the best catalytic activity, with an overpotential of only 197 mV at the current density of 10 mA cm^{-2} and Tafel slope of 39 mV dec^{-1}. Thus, this work provides an economical way to prepare efficient electrocatalysts based on transition metal elements.

Keywords: Ni_xFe_1 oxide, Amorphous, Oxygen evolution reaction, Hydrothermal

1. INTRODUCTION

With the ever-decreasing fossil fuel reserves, hydrogen production technology from electrolysis water based on renewable energy has attracted more and more attention [1-3]. Oxygen evolution reaction (OER) is a semi-reaction the kinetically rate-limiting step of water splitting. Sluggish reaction kinetics and excessive overpotential are the main bottlenecks faced by OER [4]. Although the precious metal-based catalysts IrO_2 and RuO_2 have excellent performance, the overhead cost and poor stability hinder

their wide application as commercial catalytic electrodes [5-7]. Therefore, it is urgent to find cheaper OER catalysts with high-performance other than noble metal-based catalysts. Nickel (Ni) as a rich first-row transition metal shows good corrosion resistance and ductility. At the beginning of the last century, researchers discovered that nickel and its oxides showed electrocatalytic activity for OER in alkaline solutions [9]. It is due to the electrocatalytic process mediated by oxygen compounds on the nickel surface that converts O^{2-}ions into molecular O_2. $NiO(OH)_2$ is overoxidized to $NiOO_2$, which acts as an intermediate or precursor of O_2 molecule. In a strong acid medium, H_2O_2 could play the role of O_2 precursor [8]. Iron impurities can significantly reduce the OER overpotential of nickel hydroxide ($Ni(OH)_2$) electrode, which has aroused the interests of scientists in the research of NiFe-based bimetallic materials [9]. NiFe-based bimetallic materials have been widely investigated due to their abundant reserves and good stability in the OER process, but the need to increase the active sites and reduce the overpotential is still an urgent problem [10,11]

Doping is an effective method to intentionally embed a small number of metal ions or heteroatoms into host nanomaterials. It can help to modify the electronic structure of electrocatalysts and increase electrical conductivity thereby bringing enhanced catalytic activity [12]. Xuan et al. [13] prepared amorphous Ni-Fe-O-H (H=P, B, S) nanocubes by coprecipitation method of $NiCl_2{\cdot}6H_2O$ and $K_3[Fe(CN)_6]$. Ni-Fe-O-H had a prominent porous structure, which provided many pores and channels for mass transfer and ion diffusion. The uniform distribution of heteroatom energy in the matrix leads to enhanced activity and stability of the electrocatalyst. Among them, NiFe-O-S had the best electrocatalytic activity for OER. When the current density was 10 mA cm^{-2}, the overpotential was 227 mV, and the Tafel slope was 50 mV dec^{-1}. The authors believed that P or the surrounding electronic structure could affect nickel and iron atoms, which is beneficial to the charge transfer process. The amorphous structure providing unsaturated atoms as exposed sites led to an apparent increase in active sites, which also helps to improve catalytic activity. Luo et al. [14] used $NaBH_4$'s rapid participation and kinetic control to anchor a single atom of Ir on a three-dimensional (3D) amorphous NiFe/Ni nanowire@nanosheets (NW@NSs) using a one-step method. $NiFeIr_x$/Ni $NW@NS_S$ exhibits significant OER activity in an alkaline medium. Especially for the optimized $NiFeIr_{0.03}$/Ni, the overpotential was only 200 mV at 10 mA cm^{-2}, while the Tafel slope was 45 mV dec^{-1}. Gao et al. [15] used $Ni(NO_3)_2$, $Fe(NO_3)_3$, diethyl oxalate, and nickel foam solvents to prepare nickel oxalate nanoarrays $(Ni_{1-x}Fe_x)C_2O_4$ through a simple solvothermal method. They found that compared with pure NiC_2O_4 samples, those doped with Fe significantly improved the OER performance. The OER activity increased and reached the maximum when the Fe content increased to 0.3. The reason was that, as the Fe content increased, the Ni and Fe atoms in $(Ni_{1-x}Fe_x)C_2O_4$ were gradually uniformly blended at the atomic level to form a solid solution, avoiding the formation of precipitates, and improving OER performance. Nevertheless, the phase separation of Fe and Ni gradually led to the degradation of OER performance with excessive Fe doping. When the current density was 50 and 100 mA cm^{-2}, the overpotential of $(Ni_{0.7}Fe_{0.3})C_2O_4$ was 203 mV and 243 mV, respectively, which were much lower than the overpotential of the pure NiC_2O_4. Cai et al. [16] used a two-step hydrothermal/electrodeposition method to deposit cerium oxide on nickel-iron hydroxide (NiFeCH(Ce)) on carbon fibre paper. After loading CeO_x, nickel-iron hydroxide(NiFeCH(Ce)) effectively promoted the formation of oxygen vacancies and caused lattice distortion. In addition, Ce^{3+} and Ce^{4+} could undergo redox conversion, which boosts the diffusion of

oxygen through short ion diffusion paths. It (The deposit cerium oxide) enriched the surface defects, increased oxygen adsorption capacity, and supplied a more effective charge and mass transfer between the intermediate and the catalyst. NiFeCH(Ce) has an overpotential 252 mV at 100 mA cm^{-2} with a slight Tafel slope of 59 mV dec^{-1}, showing excellent electrochemical performance.

At the same time, the construction of nanostructure electrocatalyst is an effective tool to reduce the overpotential by maximizing the surface area and exposure of catalytic active sites [17,18]. Wu et al. [19] used the self-sacrificing template and coprecipitation method to prepare ZIF-67 induced NiFe-LDH nanosheets (NiFe-LDH/ZIF-67). The advantage of the synthesized NiFe-LDH/ZIF-67 was that ZIF-67 would form a hollow nanostructure and generate many H protons during the hydrolysis process. These H protons might corrode the surrounding NiFe-LDH nanosheets and form nanopores, thus significantly increasing the specific surface area and the exposure of active sites. The experimental results were also in remarkable agreement with this hypothesis. At a current of 10 mA cm^{-2}, compared with the overpotential of 310 mV of the NiFe-LDH, the best overpotential of NiFe-LDH/ZIF-67 nanosheets was only 222 mV. In addition, the Tafel slope was also shallow, only 53 mV dec^{-1}, indicating that NiFe-LDH/ZIF-67 had good OER kinetics. Zhang et al. [20] successfully synthesized porous monolayer NiFe-LDH nanosheets (PM-LDH) with abundant defects by a one-step method. The porous monolayer structure provided a larger electroactive surface and a high concentration of defects. For example, both oxygen and metal vacancies could dramatically distort the LDH nanosheets, thereby changing their electronic properties, which causes many multi-vacancies to be exposed on the edges to improve their OER performance. When the current density was 10 mA cm^{-2}, the overpotential was 230 mV, and the Tafel slope was 47 mV dec^{-1}, respectively. Compared with the overpotential of the electrode under the same current, such as M-LDH (272mV), RM-LDH (285mV), urea LDH (304mV), IrO_2 (322mV) and graphite paper (645mV) Etc. PM-LDH exhibit more excellent OER performance.

There is no doubt that doping and nanometerization can significantly improve the OER performance of electrocatalysts. However, the mutual influence of the elements in the doping will make the synthesis process complicated. In the preparation of nanostructured catalysts, the rate of separation of bubbles on the catalyst surface determines the activity and stability of its OER [21]. Compared with the crystalline catalyst synthesized by these two methods, the amorphous catalyst has the advantages of a simple and controllable synthesis process, less restrictive conditions, providing more electrolyte transport channels and more catalytic exposed active sites. The arrangement of amorphous materials is terse, with irregular borders, composed of randomly arranged atoms. This structural feature produces many defects, which could serve as catalytically active sites, thus promoting the diffusion of ions through the catalyst layer [22,23].

Ye et al. [24] proposed a simple one-step method to electrodeposit amorphous nickel-iron (oxidized) nanosheets on a three-dimensional partially exfoliated graphite (EG) foil substrate. They found that the EG substrate had a three-dimensional layered structure, with outstanding electric conductivity and a larger surface area for catalyst deposition and O_2/ion diffusion. In addition, the strong interaction between EG and NiFe(oxy) hydroxide ensured the long-term stability of the catalyst. When Fe was incorporated, the charge transferred between the nickel and iron centers. The Ni active center has more substantial positive charge and stronger attraction to OH^-, which is beneficial to improve the catalytic activity. The incorporation of Fe also helped to change the morphology of the (oxygen)

hydroxide. Compared with the dense Ni/EG-1.2V nanosheets, the corrugated structure of NiFe/EG-1.2V nanosheets was dispersed more extensively. As increasing the Fe content, the lateral extension of the nanosheets increases. This open structure promoted mass transportation of ions and ensured outstanding OER activity even at high current densities. When the Fe concentration was too high (Ni/Fe mol ratio equaled 1:1), the formation potential of Ni (III)/Ni (IV) activation sites was too high, and it would cause the aggregation of NiFe1:1/EG-1.2V nanosheets, thus delaying the occurrence of OER. NiFe2:1/EG-1.2V shows the best catalytic performance. The OER overpotential was 214 mV at 10 mA cm^{-2}, while the Tafel slope was 21 mV dec^{-1}. Zhang et al. [25] synthesized an amorphous NiFe-LDH@NiFe-Bi/Carbon cloth. They found that the overpotential of this core-shell NiFe-LDH@NiFe-Bi/CC at 50 mA cm^{-2} in 1.0 M KOH was only 294 mV, which was 116 mV lower than NiFe-LDH/CC.

Ferric chloride and nickel chloride were used as raw materials to synthesize amorphous nickel-iron oxide by a simple one-step hydrothermal method. A citric acid-sodium citrate buffer solution (pH=5) was used to slow down crystallization, and the template CTAB [26] which formed micelles in the liquid phase was used to control the morphology. The effect of various conditions on the morphology and electrocatalytic performance of the synthesized product are discussed in detail, including buffer solution, template CTAB, and different molar ratios of nickel and iron. The process was economical and had great potential for producing nickel-iron catalysts with excellent OER performance.

2. EXPERIMENTAL SECTION

2.1. Reagents and raw materials

Nafion solution (5wt%) was purchased from Beijing Chemical Plant. Alumina (1.5μm/1.0μm/500nm) was purchased from Tianjin Aida Hengsheng Technology Development Co., Ltd. All the other chemical reagents used in this study were purchased from Sinopharm Chemical Reagent Co., Ltd. The chemicals were all analytical-grade chemicals and could be used without further purification.

2.2. Experimental method

1.0 g of CTAB was added to 30 mL citric acid-sodium citrate buffer solution (pH=5.0), which was then magnetically stirred for 30 min. After that, an appropriate amount of nickel chloride and iron chloride (Ni/Fe mol ratio equals to 2:1, 3:1, 4:1 respectively) were added to the mixed solution. After 30 minutes of magnetic stirring, the mixed solution was poured into a polytetrafluoroethylene lining. Then transferred into a stainless-steel reactor vessel, followed by a hydrothermal reaction at 140°C for 12 hours. Next, the obtained sample was washed alternately with ethanol and water to remove the surfactant. Finally, the washed sample was dried at 60 °C for 12 hours, recorded as CTAB+Cri-Ni_xFe_1. If all other steps were the same except that a citric acid-sodium citrate buffer solution was used and CTAB was not added, the prepared sample was recorded as Cri-Ni_xFe_1. If the citric acid-sodium citrate buffer solution was replaced with distilled water, CTAB was added, and the other steps remained unchanged, the sample

obtained was marked as CTAB-Ni_xFe_1. If distilled water was used and CTAB was not added, the sample obtained with the other steps unchanged was recorded as No-Ni_xFe_1.

2.3. Material characterization and testing

The powder X-ray diffraction (XRD) was examined on Bruker advanced D8 with Cu Kα radiation (40 kV, 40 mA). Transmission electron microscopy (TEM, JEM-2100F) was used to observe the morphologies of the samples at an acceleration voltage of 200 kV. The electrochemical performance test of the samples was carried out using Metrohm Autolab PGSTAT302N electrochemical workstation.

2.4. Electrochemical analysis

2.4.1. Electrode preparation

The electrode adopted in this paper was a 3 mm diameter glassy carbon electrode, which needed to be pre-treated before testing. First, it was immersed in dilute hydrochloric acid and water, respectively, and sonicated for 15 minutes. After being dried, it was sanded with 1500 grit sandpaper for 5 minutes. Then the electrode was separately polished by alumina powder of 1.5 μm, 1 μm, and 500 nm, for 5 minutes each time, and these processes were repeated twice. Finally, it was sanded with suede for 5 minutes. During the polishing procedure, the electrode was always kept perpendicular to the polishing cloth. Until the electrode was polished brightly, it was ultrasonicated with dilute hydrochloric acid, ethanol, and water for 15 minutes, respectively. Then it was dried and saved for later use. 5 mg active substance was weighed and dispersed in a mixed solution of 0.5 mL ethanol and 0.5 mL isopropanol. Then 20 μL of Nafion solution (0.5wt%) was added dropwise, and the mixed solution was ultrasonicated for 30 minutes. Finally, 5 μL solution after sonication was dripped onto the electrode surface, and it was allowed to be dried naturally for later use.

2.4.2. Electrochemical test

In this paper, the test system was a standard three-electrode system. The working electrode was a glassy carbon electrode loaded with different samples. The reference electrode and the counter electrode were Hg/HgO electrode and Pt chip electrode, respectively, and the concentration of the electrolyte was 1.0 mol/L KOH. First, 50 times cyclic voltammetry tests were performed to activate the working electrode at 0.1 V/s scan rate between 1.0-1.8 V (vs RHE) potential window. Then, the OER performance and electrocatalytic process kinetics were measured by the linear sweep voltammetry (LSV) at 0.01 V/s scan rate between 1.0-1.8 V (vs RHE) potential window. The overpotential, Tafel slope, exchange current density, and other kinetic parameters of the material were measured by LSV accordingly. Electrochemical AC impedance test was mainly used to test the internal resistance of materials and other parameters. The frequency range was 0.1 Hz-l00 kHz, and the amplitude was 5 mV.

The magnetic stirrer was kept on in order to avoid adhering of bubbles on the electrode surface during the electrochemical test.

3. RESULTS AND DISCUSSION

3.1. Structure Characterization

X-ray diffraction (XRD) results of CTAB+Cri-Ni_xFe_1 (x=2, 3, 4) were illustrated in Figure 1a. The flat diffraction peaks indicate the amorphous structure of CTAB+Cri-Ni_xFe_1(x=2, 3, 4). As demonstrated in Figure 1b, an amorphous structure with irregular borders can generate more active sites than a neatly arranged crystal structure.

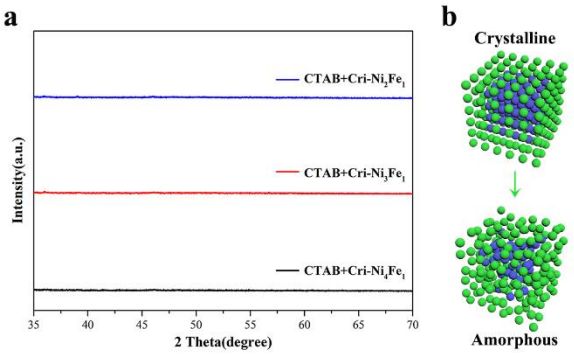

Figure 1. XRD of CTAB+Cri-Ni_xFe_1(x=2,3,4) (a); Atomic model of catalytically active sites exposed by crystalline and amorphous structures (b).

The morphology of the obtained nickel-iron oxides was characterized, as shown in Figure 2. The agglomerated NO-Ni_xFe_1 (Figure 2a, Figure 2e, Figure 2i) samples were produced in distilled water, with a diameter of up to 1 μm (Figure 2a). Amorphous particles have high surface reaction activity, which will result in solid adsorption capacity. In addition, the particle size of iron oxide particles will increase significantly in the range around $pH_{IEP} \approx 7.8$ (the isoelectric point), and agglomeration is accessible to occur [27].

The surface charge of particles is usually expressed by zeta potential. The absolute value of the zeta potential of particles tends to increase as pH moves away from pH_{IEP}. Particles are easily agglomerated by van der Waals force near pH_{IEP}, because of the weak repulsive force between the electrical double layers of particles which caused by the low surface charge density of particles [28,29].

Under the condition of pH = 4-5, which is far away from pH_{IEP}, resulting in a relative weakening of agglomeration behavior of iron oxide particles [27]. At the same time, the presence of Na^+ and Cl^- make citric acid stick on the surface of iron oxide particles which helps to prevent agglomeration [30]. Therefore, the Cri-Ni_xFe_1 (Figure 2b, Figure 2f, Figure 2j) had a significantly reduced agglomerate particle size, with the minor agglomerate diameter of approximately 50 nm (Figure 2j).

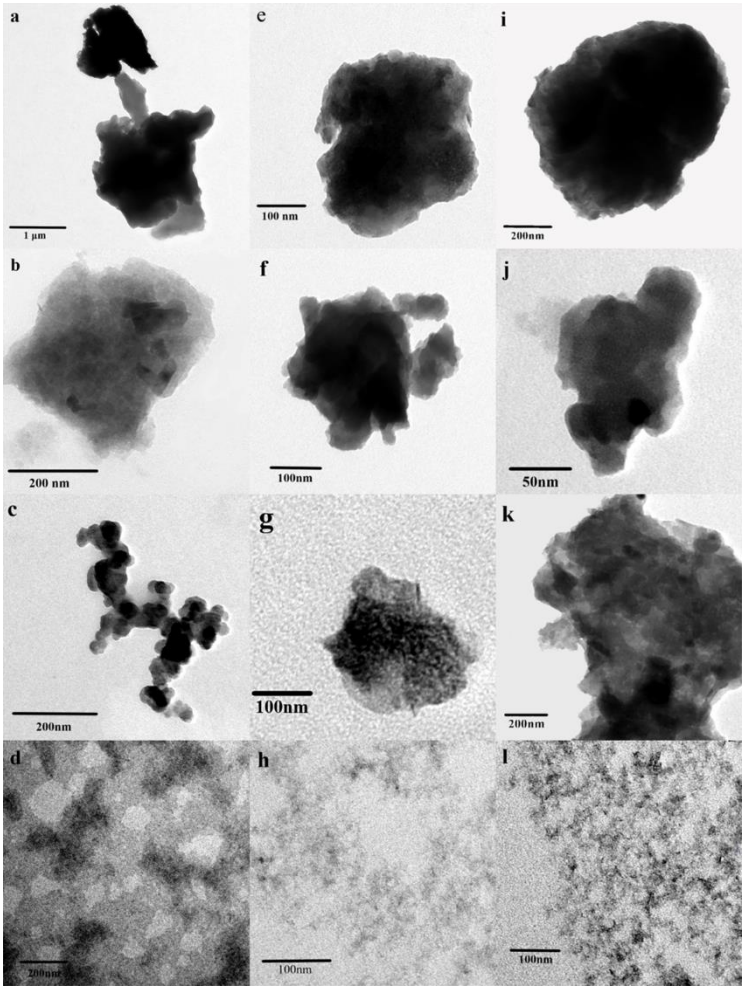

Figure 2. TEM images of No-Ni_xFe_1 (x=2, 3, 4) (a, e, i); TEM images of Cri-Ni_xFe_1 (x=2, 3, 4) (b, f, j) ; TEM images of CTAB-Ni_xFe_1 (x=2, 3, 4) (c, g, k); TEM images of CTAB+Cri-Ni_xFe_1(x=2, 3, 4) (d, h, l).

However, it was still tightly aggregated, and no porous structure appeared. The product CTAB-Ni_xFe_1 (Figure 2c, Figure 2g, Figure 2k) was similar to the product (Cri-Ni_xFe_1) prepared by using buffer solution. As we all know, CTAB can form micelles in the solution, thereby affecting the spatial confinement of the ordered aggregates formed by molecules, then controlling the formation of particles. Nevertheless, it was still insufficient to disperse the amorphous nickel-iron oxide in this work. CTAB+Cri-Ni_xFe_1 (Figure 2d, Figure 2h, Figure 2l) generated under the combined effects of buffer solution (pH=5) and CTAB, and formed amorphous Ni-Fe oxide floc with a large number of pores. When Ni/Fe mol ratio equaled 3:1, the dispersibility of the Ni-Fe oxide generated was the best, which significantly increased the exposure of its active sites (Figure 3).

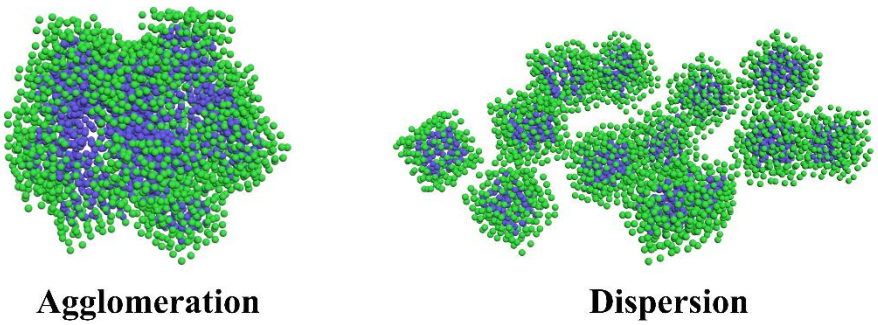

Figure 3. Atomic model of catalytically active sites exposed by agglomeration and dispersion

3.2. Analysis of OER Electrocatalytic Activity

In order to verify the electrochemical activity of this amorphous porous structure, the OER electrocatalytic activities were analyzed in detail. Figure 4a shows the linear volt-ampere curves of No-Ni_2Fe_1, CTAB-Ni_2Fe_1, Cri-Ni_2Fe_1, CTAB+Cri-Ni_2Fe_1, respectively. The initial potential of No-Ni_2Fe_1, Cri-Ni_2Fe_1, CTAB-Ni_2Fe_1 samples were all around 1.58 V. The initial potential of CTAB+Cri-Ni_2Fe_1 was around 1.36 V. At the same potential of 1.8 V, the current densities corresponded to No-Ni_2Fe_1, CTAB-Ni_2Fe_1, Cri-Ni_2Fe_1, CTAB+Cri-Ni_2Fe_1 were 1.52 mA cm^{-2}, 2.98 mA cm^{-2}, 22.4 mA cm^{-2}, 33.7 mA cm^{-2}, respectively. When the current density was 10 mA cm^{-2}, the overpotential of CTAB+Cri-Ni_2Fe_1 was 334 mV, and Cri-Ni_2Fe_1 was 516 mV. For the other two samples, the current densities did not reach 10 mA cm^{-2}, which suggested their electrocatalytic activity was bad. The Tafel slopes of No-Ni_2Fe_1, Cri-Ni_2Fe_1, CTAB-Ni_2Fe_1, CTAB+Cri-Ni_2Fe_1 were separately demonstrated in Figure 4b, and the order was CTAB+Cri-Ni_2Fe_1 (85mV dec^{-1}) < Cri-Ni_2Fe_1 (128mV dec^{-1}) < CTAB-Ni_2Fe_1 (264mV dec^{-1}) < No-Ni_2Fe_1 (392mV dec^{-1}), indicating that CTAB+Cri-Ni_2Fe_1 electrocatalyst had the fastest electrode reaction. Figure 4c demonstrated the Nyquist diagrams of No-Ni_2Fe_1, CTAB-Ni_2Fe_1, Cri-Ni_2Fe_1, CTAB+Cri-Ni_2Fe_1, respectively. Approximately circular arcs confirmed that the electrode reaction was electrochemically controlled. The equivalent circuit diagram of curve fitting in Figure 3c can be seen as three parts: R_s (dissolved s-liquid resistance), R_{ct} (charge transfer resistance at the electrode/solution interface), and CPE (constant phase angle element). Among them, resistance (R_{ct}) is the main factor which affect the electrocatalytic performance of the material. From Table 1, the charge transfer resistance of CTAB+Cri-Ni_2Fe_1 was 23.8 times lower than that of No-Ni_2Fe_1, so CTAB+Cri-Ni_2Fe_1 had a better electrocatalytic performance. It was mainly contributed to changes in morphology and structure. By gradually changing the sample into porous floc may promote the electron flow between the sample and the electrolyte.

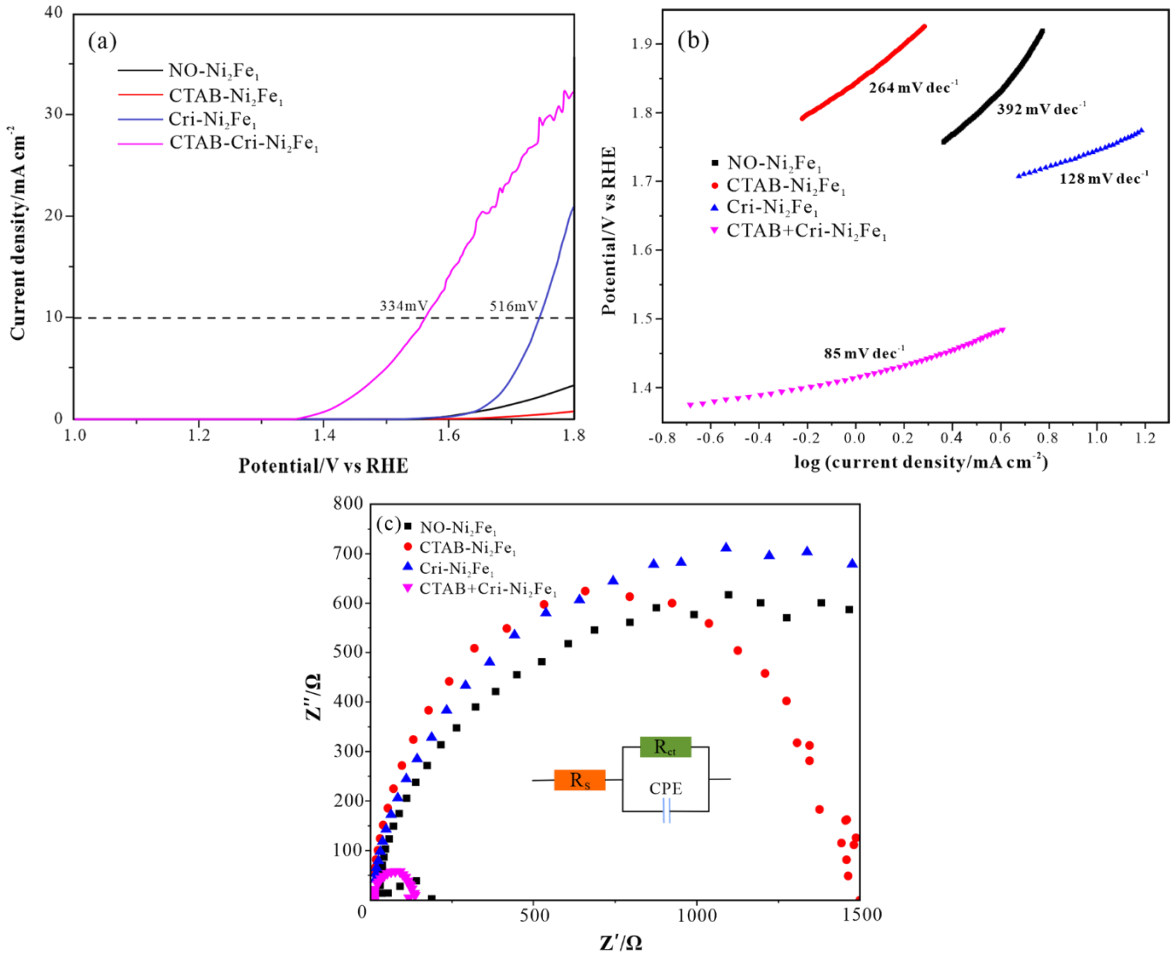

Figure 4. No-Ni_2Fe_1, CTAB-Ni_2Fe_1, Cri-Ni_2Fe_1, CTAB+Cri-Ni_2Fe_1 linear volt-ampere curve (a); No-Ni_2Fe_1, CTAB-Ni_2Fe_1, Cri-Ni_2Fe_1, CTAB+Cri-Ni_2Fe_1 Tafel Slope (b); Nyquist diagrams of No-Ni_2Fe_1, CTAB-Ni_2Fe_1, CriNi_2Fe_1, CTAB+Cri-Ni_2Fe_1 (c), the inset is the equivalent circuit obtained by fitting the curve.

Table 1. Fitted value of Rct in the equivalent circuit of No-Ni_2Fe_1, CTAB-Ni_2Fe_1, Cri-Ni_2Fe_1, CTAB+Cri-Ni_2Fe_1, respectively.

sample	No-Ni_2Fe_1	CTAB-Ni_2Fe_1	Cri-Ni_2Fe_1	CTAB+Cri-Ni_2Fe_1
R_{ct}/Ω	2110	1490	1130	85

Figure 5a gave the linear volt-ampere curves of No-Ni_3Fe_1, CTAB-Ni_3Fe_1, Cri-Ni_3Fe_1, CTAB+Cri-Ni_3Fe_1, respectively. The starting potential of CTAB+Cri-Ni_3Fe_1 was the lowest, only 1.36 V. At the same potential of 1.8 V, the current density corresponding to CTAB+Cri-Ni_3Fe_1 was the largest. When the current density was 10 mA cm^{-2}, the overpotential of CTAB+Cri-Ni_3Fe_1 was only 197 mV, and the catalytic performance was the best. As shown in Figure 5b, the Tafel slope of CTAB+Cri-Ni_3Fe_1 was also the lowest, at 39 mV dec^{-1}. Table 2 illustrated the comparison of its OER performance

and preparation process with some other similar electrocatalyst. It might be that the formation of peroxide (HOO) or peroxy (OO) intermediates limited the rate of the Tafel slope of 39 mV dec^{-1} on the aqueous iron oxide film in the alkaline electrolyte [31]. At the same time, the amorphous nickel-iron alloy catalyst could expose internal active sites by applying an anode potential, thereby significantly improving its electrochemical activation ability and water oxidation activity [32]. Figure 4c demonstrated the Nyquist diagrams of No-Ni_3Fe_1, CTAB-Ni_3Fe_1, Cri-Ni_3Fe_1, CTAB+Cri-Ni_3Fe_1, respectively. Figure 4d is the dashed frame part in Figure 5c. The approximate circular arc line still confirmed that the electrode reaction was electrochemically controlled.

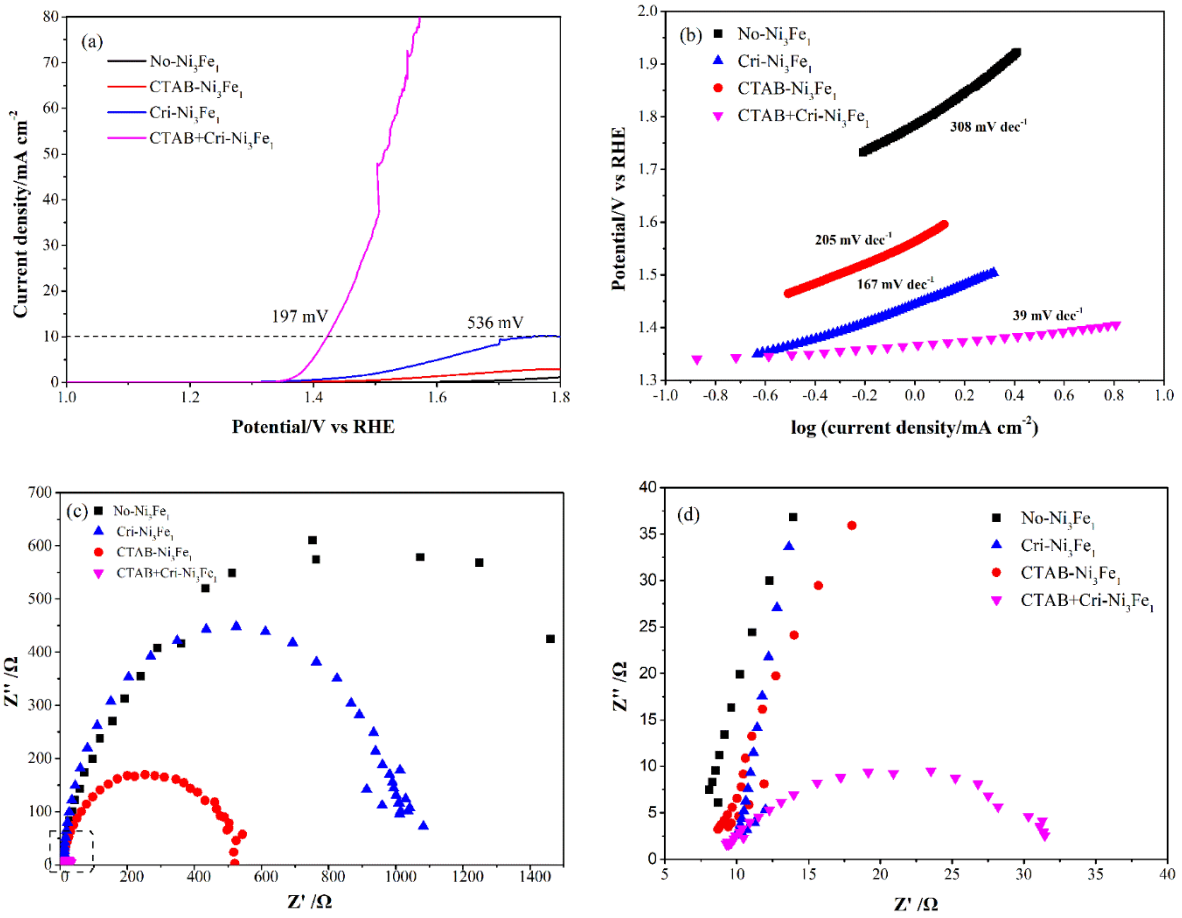

Figure 5. No-Ni_3Fe_1, CTAB-Ni_3Fe_1, Cri-Ni_3Fe_1, CTAB+Cri-Ni_3Fe_1 linear volt-ampere curve (a); No-Ni_3Fe_1, CTAB-Ni_3Fe_1, Cri-Ni_3Fe_1, CTAB+Cri-Ni_3Fe_1 Tafel Slope (b); Nyquist plots of No-Ni_3Fe_1, CTAB-Ni_3Fe_1, Cri-Ni_3Fe_1, CTAB+Cri-Ni_3Fe_1 (c); (d) is the dashed frame part in Figure (c).

Table 2 Overview of the preparation and performance of some NiFe-based bimetallic catalysts

Category	Crystal structure	Electrocatalyst	Catalytic performance			Processed	Reference
			Current density (mA)	OER overpotential (mV)	Tafel slope (mV dec^{-1})		
Doping	Amorphous	Ni-Fe-O-H (H=P, B, S)	10	227	50	MOFs (NiFe-PBA was first prepared by a coprecipitation method. Then $NH_4H_2PO_4$, H_3BO_3, or thiourea were mixed with the precursor and sintered at 450 °C for 5 h.	Xuan et al. [13]
	Amorphous	$NiFeIr_{0.03}$/Ni NW@NSs	10	200	45	$NaBH_4$ reduced high concentrations of Ni, Fe, and Ir ions in one step to form $NiFeIr_x$/Ni NW@NSs.	Luo et al. [14]
	Crystals	$(Ni_{0.7}Fe_{0.3})C_2O_4$	50	203	43	$(Ni_{1-x}Fe_x)C_2O_4$ was prepared by one-step solvothermal synthesis by nickel oxalate and iron oxalate	Gao et al. [15]
Nanostructure	Crystals	NiFeCH(Ce)	100	252	59	First, the precursor NiFeCH was prepared by hydrothermal reaction of nickel nitrate and ferrous ammonium sulfate at 120℃ for 10h. Next, the precursor NiFeCH was subjected to CeO_x electrodeposition in a 2 mM $Ce(NO_3)_3$ + 10 mM NaCl solution.	Cai et al. [16]
	Crystals	NiFe-LDH/ZIF-67	10	222	53	ZIF-67 was first synthesized by the solvothermal method, and then NiFe-LDH/ZIF-67 was prepared by the coupling method of a self-sacrificial template and coprecipitation methods.	Wu et al. [19]
	Crystals	PM-LDH	10	230	47	Ni^{2+} and Fe^{3+} aqueous solutions were added dropwise to 80°C formamides aqueous solution (pH=10) to synthesize monolayer NiFe-LDH nanosheets	Zhang et al. [20]
Nanostructure	Crystals	NiO/C@NiFe-LDH	10	299	45	Ni-MOFs were first synthesized by the hydrothermal method, calcined at 900°C for 2h to obtain Ni/NiO/C. Finally, Ni/NiO/C was synthesized into NiO/C@NiFe-LDH by hydrothermal method.	Li et al. [33]
Amorphous	Amorphous	Ni/EG-1.2V	10	214	21	Ni/EG-1.2V was prepared by electrodepositing amorphous NiFe (oxygen) hydroxide on a three-dimensional partially exfoliated graphite foil substrate (EG).	Ye et al. [24]
	Amorphous	NiFe-LDH@NiFe-Bi/CC	50	294	96	NiFe-LDH@NiFe-Bi/CC was prepared by introducing amorphous NiFe-Bi on the surface of NiFe-LDH.	Zhang et al. [25]
	Amorphous	$NiFe_2O_4$/NiFe $(OH)_x$	10	276	68	$NiFe_2O_4$ was prepared by hydrothermal method, which was ultra-sonicated in $NaBH_4$ solution for 1 minute to obtain $NiFe_2O_4$/NiFe$(OH)_x$.	Yao et al. [34]
In this research	Amorphous	CTAB+Cri-Ni_3Fe_1	10	197	39	CTAB+Cri-Ni_3Fe_1 was synthesized by a one-step hydrothermal method using ferric chloride and nickel chloride in a citric acid-sodium citrate buffer solution (pH=5) added with the template CTAB.	

It could be seen from Table 3 that the charge transfer resistance of CTAB+Cri-Ni_3Fe_1 was 60.3 times lower than that of No-Ni_3Fe_1, so CTAB+Cri-Ni_3Fe_1 had the best electrocatalytic performance, followed by Cri-Ni_3Fe_1 (500Ω).

Table 3. Fitted value of Rct in the equivalent circuit of No-Ni_3Fe_1, CTAB-Ni_3Fe_1, Cri-Ni_3Fe_1, CTAB+Cri-Ni_3Fe_1, respectively.

sample	No-Ni_3Fe_1	CTAB-Ni_3Fe_1	Cri-Ni_3Fe_1	CTAB+Cri-Ni_3Fe_1
Rct/Ω	1980	1040	500	32.3

The linear volt-ampere curves of No-Ni_4Fe_1, CTAB-Ni_4Fe_1, Cri-Ni_4Fe_1, CTAB+Cri-Ni_4Fe_1 were illustrated in Figure 6a, respectively. The initial potential of the CTAB+Cri-Ni_4Fe_1 sample was about 1.35 V, which was nearly 300 mV lower than the initial voltage of the other three samples. At the same potential of 1.8 V, the current density of CTAB+Cri-Ni_4Fe_1 was the largest. At a current density of 10 mA cm^{-2}, the overpotential of CTAB+Cri-Ni_4Fe_1 was only 221 mV. According to Figure 6b, the Tafel slope was 53 mV dec^{-1}.

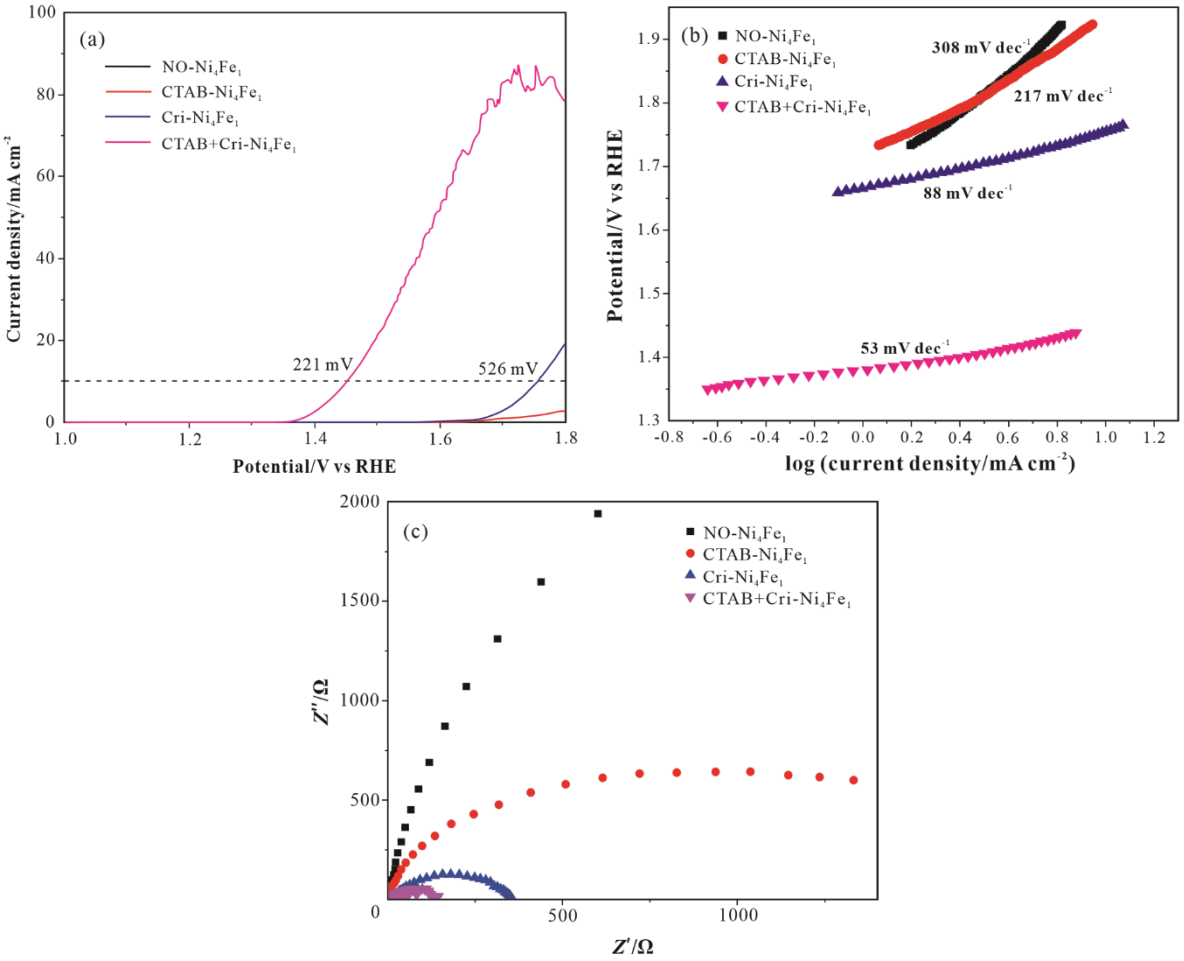

Figure 6. No-Ni_4Fe_1, CTAB-Ni_4Fe_1, Cri-Ni_4Fe_1, CTAB+Cri-Ni_4Fe_1 linear volt-ampere curve (a); No-Ni_4Fe_1, CTAB-Ni_4Fe_1, Cri-Ni_4Fe_1, CTAB+Cri-Ni_4Fe_1 Tafel Slope (b); Nyquist plot of No-Ni_4Fe_1, CTAB-Ni_4Fe_1, Cri-Ni_4Fe_1, CTAB+Cri-Ni_4Fe_1 (c).

The catalytic performance of CTAB+Cri-Ni_4Fe_1 was between that of CTAB+Cri-Ni_2Fe_1 and that of CTAB+Cri-Ni_3Fe_1. The reason might be that as the Fe concentration increased, the Ni and Fe elements in CTAB+Cri-Ni_xFe_1 would gradually uniformly mix at the atomic level, and the charge transfer between the Ni and Fe centers led to changes in the electronic structure of Ni, thereby improving its OER performance. When Ni/Fe mol ratio equaled 3:1, the catalytic performance was the best. However, when the concentration of Fe continued to increase, it would cause excessive Fe in CTAB+Cri-Ni_xFe_1, and the Fe phase and Ni phase would gradually separate. The formation potential of Ni (III)/Ni (IV) activation sites was too enormous, which would reduce its OER performance to a large extent [15,24]. Figure 6c demonstrated the Nyquist diagrams of No-Ni_4Fe_1, CTAB-Ni_4Fe_1, Cri-Ni_4Fe_1, CTAB+Cri-Ni_4Fe_1, respectively. The approximate circular arc line also confirmed that the electrode reaction was electrochemically controlled.

It could be seen from Table 4 that the charge transfer resistance of CTAB+Cri-Ni_4Fe_1 is 49.8 times lower than that of No-Ni_4Fe_1, so CTAB+Cri-Ni_4Fe_1 had the best electrocatalytic performance, followed by Cri-Ni_4Fe_1 (357Ω). Interestingly, the resistance of CTAB+Cri-Ni_xFe_1 (x=2, 3, 4) had a consistent ordering with the overpotential, which further proved the previous analysis results.

Table 4. Fitted value of Rct in the equivalent circuit of No-Ni_4Fe_1, CTAB-Ni_4Fe_1, Cri-Ni_4Fe_1, CTAB+Cri-Ni_4Fe_1, respectively.

sample	No-Ni_4Fe_1	CTAB-Ni_4Fe_1	Cri-Ni_4Fe_1	CTAB+Cri-Ni_4Fe_1
R_{ct}/Ω	2980	1920	357	58.6

4. CONCLUSION

In summary, the amorphous nickel-iron oxide catalysts were successfully prepared by the hydrothermal synthesis method. Surprisingly, for the newly developed CTAB+Cri-Ni_3Fe_1 catalyst, the overpotential at 10 mA cm^{-2} was only 197 mV, and the Tafel slope was 39 mV dec^{-1}, one of the best OER catalytic performances among the current reports. During the synthesis, the crystallinity and agglomeration of CTAB+Cri-Ni_xFe_1 were suppressed under the combined action of templating agent CTAB and citric acid-sodium citrate buffer solution (pH=5). An amorphous matrix filled with pores was formed, greatly enhancing the exposure of catalytically active sites. Furthermore, changing the mole ratio of Ni/Fe helps to control the mixing degree of Ni-Fe, adjust the electronic structure of Ni, and make the Ni active center more positive. Therefore, the OER performance of the synthesized products was miraculously enhanced. This work provides a low-cost method for preparing high-performance catalysts based on transition metal elements.

ACKNOWLEDGEMENTS
All the authors gratefully acknowledged the financial support from the National Natural Science Foundation of China [Grant number 40802013] and the Fundamental Research Funds for the Central Universities [Grant number 2652015092].

References

1. X. X. Zou and Y. Zhang. *Chem. Soc. Rev*. 44 (2015) 5148-5180. https://doi.org/10.1039/c4cs00448e.
2. S. Chen, J. J. Duan, P. J. Bian, Y. H. Tang, R. K. Zheng and S. Z. Qiao. *Adv. Energy Mater.* 5 (2015) 1500936. https://doi.org/10.1002/aenm.201500936.
3. J. Li, J. Zheng, X. Cheng, G. Yue and X. Luo. *J. Solid State Chem*. 278 (2019) 120881. https://doi.org/10.1016/j.jssc.2019.07.042.
4. S. F. Fu, J. H. Song, C. Z. Zhu, G. L. Xu, K. Amine, C. J. Sun, X. L. Li, M. H. Engelhard, D. Du and Y. H. Lin. *Nano Energy*. 44 (2018) 319-326. https://doi.org/10.1016/j.nanoen.2017.12.010.
5. R. Frydendal, E. A. Paoli, B. P. Knudsen, D. B. Wickman, D. P. Malacrida, P. I. E. L. Stephens and P. I. Chorkendorff. *ChemElectroChem*. 1 (2014) 2075-2081. https://doi.org/10.1002/celc.201402262.
6. Y. Lee, J. Suntivich, K. J. May, E. E. Perry and Y. *J. Phys. Chem. Lett*. 3 (2013) 399-404. https://doi.org/10.1021/jz2016507.
7. T. Reier and P. M. Oezaslan, *Strasser, ACS Catal*. 2 (2012) 1765-1772. https://doi.org/10.1021/cs3003098.
8. K. Juodkazis, J. Juodkazytė, R. Vilkauskaitė and V. Jasulaitienė. *J. Solid State Electrochem*. 12 (2018) 1469-1479. https://doi.org/10.1007/s10008-007-0484-0.
9. M. Gong and H. J. Dai. *Nano Res*. 8 (2015) 23-39. https://doi.org/10.1007/s12274-014-0591-z.
10. J. Mohammed-Ibrahim. *J. Power Sources*. 448 (2020) 227375. https://doi.org/10.1016/j.jpowsour.2019.227375.
11. L. Gong, H. Yang, A. I. Douka, Y. Yan and B. Y. Xia. *Adv. Sustainable Syst*. 5 (2021) 2000136. https://doi.org/10.1002/adsu.202000136.
12. J. X. Wu, Z. Y. Pan, Y. Zhang, B. J. Wang and H. S. Peng. *J. Mater. Chem. A*. 6 (2018) 12932-12944. https://doi.org/10.1039/c8ta03968b.
13. C. J. Xuan, J. Wang, W. W. Xia, J. Zhu, Z. K. Peng, K. D. Xia, W. P. Xiao, H. L. L. Xin and D. L. Wang. *J. Mater. Chem. A*. 16 (2018) 7062-7069. https://doi.org/10.1039/C8TA00410B.
14. X. Luo, X. Q. Wei, H. Zhong, H. J. Wang, Y. Wu, Q. Wang, W. L. Gu, M. Gu, S. P. Beckman and C. Z Zhu. *ACS Appl. Mater. Interfaces*. 12 (2020) 3539-3546. https://doi.org/10.1021/acsami.9b17476.
15. X. Gao, D. Chen, J. Qi, F. Li, Y. Song, W. Zhang and R. Cao. *Small*. 15 (2019) e1904579. https://doi.org/10.1002/smll.201904579.
16. J. H. Cai, J. G. Huang, S. C. Xu, L. Yuan, X. R. Huang, Z. P. Huang and C. Zhang. *J. Solid State Electrochem*. 23 (2019) 3449-3458. https://doi.org/10.1007/s10008-019-04445-9.
17. H. A. Bandal, A. R. Jadhav, A. A. Chaugule, W-J. Chung and H. Kim. *Electrochim. Acta*. 222 (2016) 1316-1325. https://doi.org/10.1016/j.electacta.2016.11.107.
18. Y. X. Zhang, X. Guo, X. Zhai, Y. M. Yan and K. N. Sun. *J. Mater. Chem. A*. 3 (2015) 1761-1768. https://doi.org/10.1039/c4ta04641b.
19. W. Wu, J. Liu, G. Chen, Y. Chen and C. L. Xu. *Int. J. Hydrogen Energy*. 45 (2020) 1948-1958. https://doi.org/10.1016/j.ijhydene.2019.11.108.
20. X. Zhang, Y. F. Zhao, Y. X. Zhao, R. Shi, G. I. N. Waterhouse and T. Zhang. *Adv. Energy Mater*. 9 (2019) 1-7. https://doi.org/10.1002/aenm.201900881.
21. T. T. Gao, Z. Y. Jin, M. Liao, J. L. Xiao, H. Y. Yuan and D. Xiao. *J. Mater. Chem. A*. 3 (2015) 17763-17770. https://doi.org/10.1039/c5ta04058b.
22. J. W. Lang, L. B. Kong, M. Liu, Y. C. Luo and L. Kang. *J. Electrochem. Soc*. 157 (2010) A1341-A1346. https://doi.org/10.1149/1.3497298.
23. M. Xing, L. B. Kong, M. C. Liu, L. Y. Liu, L. Kang and Y. C. Luo. *J. Mater. Chem. A*. 2 (2014) 18435-18443. https://doi.org/10.1039/c4ta03776f.
24. Y. J. Ye, N. Zhang and X. X. Liu. *J. Mater. Chem. A*. 5 (2017) 24208-24216.

https://doi.org/10.1039/C7TA06906E.
25. L. Zhang, R. Zhang, R. X. Ge, X. Ren, S. Hao, F. Y. Xie, F. L. Qu, Z. Liu, G. Du, A. M. Asiri, B. Z. Zheng and X. P. Sun. *Chem. - Eur. J.* 23 (2017) 11499-11503. https://doi.org/10.1002/chem.201702745.
26. B. Dka and Mar. C. *J. Mol. Liq*. 274 (2019) 639-645. https://doi.org/10.1016/j.molliq.2018.11.035.
27. M. Baalousha. *Sci. Total Environ*. 407 (2009) 2093-2101. https://doi.org/10.1016/j.scitotenv.2008.11.022.
28. E. Tombácz, I. Y. Tóth, D. Nesztor, E. Illes, A. Hajdu, M. Szekeres and L. Vekas. *Colloids Surf., A* 435 (2013) 91-96. https://doi.org/10.1016/j.colsurfa.2013.01.023.
29. C. Peng, C. S. Shen, S. Y. Zheng, W. L. Yang, H. Hu, J. S. Liu and J. Y. Shi. *Nanomaterials*. **7** (2017) 2079-4991. https://doi.org/10.3390/nano7100326.
30. K. Afshinnia and M. Baalousha. *Sci. Total Environ*. 581 (2017) 268-276. https://doi.org/10.1016/j.scitotenv.2016.12.117.
31. A. Alobaid, C. Wang and R. A. Adomaitis. *J. Electrochem. Soc*. 165 (2018) J3395-J3404. https://doi.org/10.1149/2.0481815jes.
32. W. Z. Cai, R. Chen, H. B. Yang, H. B. Tao, H. Y. Wang, J. J. Gao, W. Liu, S. Liu, S. F. Hung and B. Liu. Nano *Lett*. 20 (2020) 4278-4285. https://doi.org/10.1021/acs.nanolett.0c00840.
33. L. Zhang, R. Zhang, R. X. Ge, X. Ren, S. Hao, F. Y. Xie, F. L. Qu, Z. Liu, G. Du, A. M. Asiri, B. Z. Zheng, X. P. Sun. *Chem. - Eur. J.* 23 (2017) 11499-11503. https://doi.org/10.1002/chem.201702745.
34. L. Yao, Z. B. Geng, W. Zhang, X. F. Wu, J. H. Liu, L. P. Li, X. Y. Wang, X. Y. Hou, K. Xu, K. K. Huang and S. H. Feng. *ACS Sustainable Chem. Eng.* 8 (2020) 17194-17200.
35. https://doi.org/10.1021/acssuschemeng.0c05888.